nature materials

Article

https://doi.org/10.1038/s41563-026-02574-x

All-van der Waals microcavities for low-loss nonlinear photonics

Received: 12 June 2025

Accepted: 9 March 2026

Published online: 13 April 2026

Check for updates

Zhi-Yan Wang[1,5], Xiaoqi Cui[2,5], Andreas C. Liapis[2,5], Hao-Ran Shao[1,5], Xu Cheng[2,5], Jingnan Yang[2,5], Nianze Shang[2], Weizhe Zhang[1], Henri Kaaripuro[2], Juan C. Arias Muñoz[2], Kaifeng Lin[1], Wenjing Liu[1,3], Kaihui Liu[1], Qihuang Gong[1], Zhipei Sun[2] ✉ & Yun-Feng Xiao[1,3,4] ✉

Van der Waals (vdW) materials have emerged as a promising platform for next-generation nanophotonics and optoelectronics. However, employing vdW materials as a core photonic integration platform, rather than as passive or active overlays on conventional silicon-based platforms, remains challenging, leaving their full potential untapped. Here we develop a nanofabrication strategy that enables high-resolution patterning across a broad range of vdW materials, including insulators, semiconductors, ferroelectrics and their heterostructures, and we show that they can be used as the intrinsic platform for low-loss microcavity nonlinear photonic devices such as microdisks, photonic crystals and metasurfaces. We demonstrate vdW microdisk resonators with quality (Q) factors exceeding 10^6. Such Q factors enable efficient continuous-wave nonlinear optical processes, including second-harmonic generation, sum-frequency generation and optical parametric amplification, with full free-spectral-range thermal tunability. These results position vdW materials as key material building blocks for next-generation integrated photonics and optoelectronics.

Van der Waals (vdW) materials, composed of atomically thin layers bound by weak interlayer forces[1,2], rose to prominence after the groundbreaking isolation of graphene, which was a transformative milestone in materials science. Over the past two decades, this diverse material family has served as a fertile platform for both fundamental discoveries and technological innovation[1–3], owing to its distinctive optical[4], electrical[5], thermal[6] and mechanical[7] properties. In photonics, vdW materials have shown great promise due to their unique optical and electronic properties, such as strong optical nonlinearities[8,9], pronounced excitonic resonances[10] and tunable refractive indices[11]. These features have facilitated breakthroughs in light emission[12,13], frequency conversion[14], optical modulation[11], polaritonic phenomena[15], photodetection[16] and spectroscopy[17,18]. In parallel, it is a continuing priority in integrated photonics to consolidate diverse optical functionalities (for example, nonlinear optical processing, amplification and modulation) onto a single chip as part of the progress towards the development of photonic integrated circuits[19]. In this context, vdW materials provide a compelling materials library for on-chip photonics[20,21], as illustrated in Fig. 1a. Their atomically flat surfaces minimize optical scattering losses, and their unmatched compatibility with heterogeneous integration enables the construction of complex, vertically stacked architectures without lattice-matching constraints. Moreover, their extensive material library offers unprecedented flexibility for tailoring photonic and optoelectronic functions, further amplifying their appeal for highly integrated multifunctional systems.

Despite their considerable promise, existing approaches have largely confined vdW materials to auxiliary roles—typically as coated or embedded functional layers on top of conventional integrated

[1]State Key Laboratory for Mesoscopic Physics and Frontiers Science Centre for Nano-optoelectronics, School of Physics, Peking University, Beijing, China. [2]Department of Electronics and Nanoengineering, Aalto University, Espoo, Finland. [3]Collaborative Innovation Centre of Extreme Optics, Shanxi University, Taiyuan, China. [4]New Cornerstone Science Laboratory, School of Physics, Peking University, Beijing, China. [5]These authors contributed equally: Zhi-Yan Wang, Xiaoqi Cui, Andreas C. Liapis, Hao-Ran Shao, Xu Cheng, Jingnan Yang. ✉e-mail: zhipei.sun@aalto.fi; yfxiao@pku.edu.cn

https://doi.org/10.1038/s41563-026-02574-x

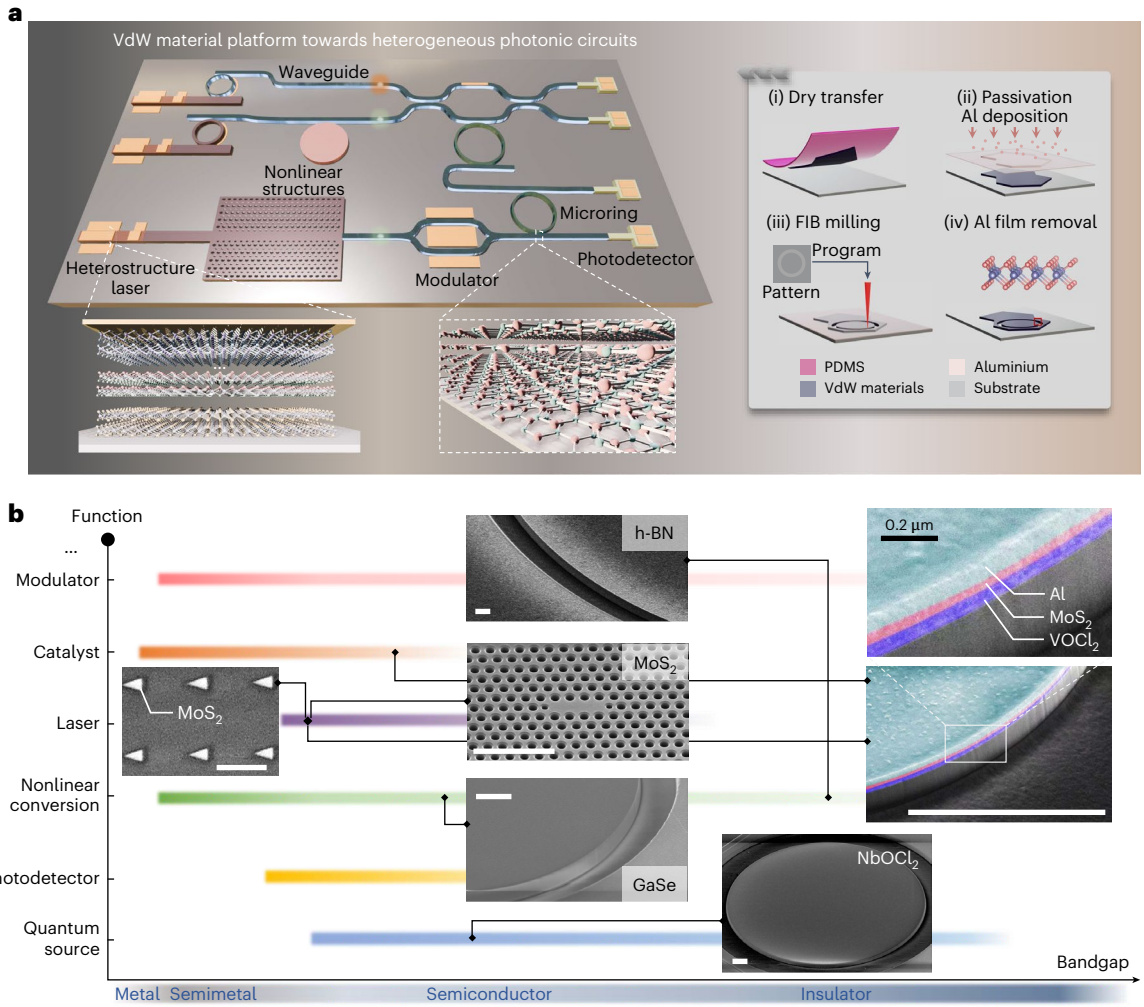

Fig. 1 | All-vdW microcavity photonics. a, Visionary conceptual illustration of a heterogeneous photonic chip based on vdW materials. It demonstrates the integration of exclusively vdW materials through techniques such as transferring, stacking and patterning, which enables the fabrication of lasers, modulators, waveguides, photodetectors and so on. Inset: fabrication workflow based on FIB milling with Al passivation. **b**, Various nanostructures fabricated from representative vdW materials (for example, h-BN, MoS_2, GaSe and $NbOCl_2$), including microdisk cavities, arrays of triangular microresonators and photonic crystal cavities. The structures span materials with different bandgaps and include heterostructure examples (for example, a $VOCl_2/MoS_2$ stack). Scale bars, 2.5 μm.

photonic platforms—rather than employing them as structural building blocks. For example, graphene has been embedded as gate-tunable dispersive elements[22] and nonlinear optical coatings[23] in integrated photonics. Transition-metal dichalcogenide layers have been transferred onto silicon-based integrated devices to enable high-performance photodetection[24] and modulation[25]. Although these studies highlight the substantial potential of vdW materials in nanophotonics and optoelectronics, their role remains largely limited and their full capacity for enabling next-generation photonic systems has yet to be realized.

Here we establish vdW materials as a viable material platform for low-loss nonlinear photonics. We introduce a generally applicable nanofabrication strategy based on focused ion beam (FIB) lithography with aluminium (Al) passivation, which enables high-resolution patterning across a broad range of vdW materials and their heterostructures. This method facilitates the fabrication of essential photonic components—including photonic crystals, metasurfaces, and microdisks—with nanometre-scale precision and well-preserved material quality to support high-quality integrated photonics. Of particular note, the fabricated microcavities support whispering gallery modes (WGMs) with quality (Q) factors exceeding 10^6, spanning from the telecom to the visible regimes. These high-Q cavity resonance modes, combined with the strong intrinsic optical nonlinearity of vdW materials, enable highly efficient nonlinear optical processes, even under continuous-wave (CW) excitation, including second-harmonic generation (SHG), sum-frequency generation (SFG) and optical parametric amplification (OPA). Notably, the normalized SHG conversion efficiency is enhanced by four orders of magnitude compared with previously reported vdW-materials systems, and the generated signal is tunable over a full free spectral range (FSR). Our results establish a design paradigm for on-chip nonlinear photonics and position vdW materials not as supplementary layers but as potential foundational platforms for high-performance photonic circuits, with promising applications in reconfigurable photonics, nonlinear signal processing and quantum technologies.

Fabrication of vdW microstructures and nanostructures for microcavity photonics

Diverse vdW materials provide a versatile platform for photonic and optoelectronic applications, with the promise of delivering tailored solutions beyond the limits of conventional monolithic photonics. With bandgaps spanning 0–6 eV, the vdW-materials family encompasses metals (for example, MXenes), semiconductors (for example, MoS_2

and WS_2) and insulators (for example, hexagonal boron nitride (h-BN)), thus enabling tailored heterostructures for diverse functionalities. Semiconducting transition-metal dichalcogenides exhibit high refractive indices advantageous for miniaturized photonic devices[26–33]. Many vdW materials also demonstrate superior nonlinear optical properties compared with traditional platforms like lithium niobate, with exceptionally high second- and third-order nonlinear optical susceptibilities (for example, GaSe and $NbOCl_2$). These attributes potentially facilitate heterogeneous integration and empower new device designs beyond the reach of conventional photonic integrated circuits.

Notwithstanding these advantages, fabricating vdW materials into nanostructures suitable for photonic integration remains technically challenging. Standard top-down approaches—including electron-beam lithography followed by reactive-ion etching[34] or direct femtosecond laser ablation[35]—often suffer from poor material compatibility. For reactive-ion etching, etching selectivity and surface quality are the main limitations due to the chemical inertness of certain vdW compounds. For example, fluorine-based gases, such as CF_4, CHF_3 and SF_6, are effective in etching Mo- and W-based dichalcogenides (for example, refs. 27,28,34,36–38), but they are almost non-reactive with some XSe (where X = In, Ga and so on). This lack of reactivity leads to limited etch selectivity against photoresists and hard masks, resulting in poorly defined sidewalls and substantially hampering the ability to create clean, high-resolution optical structures. Femtosecond laser ablation, although material-agnostic in principle, introduces thermal damage and surface roughening, which degrades both structural and optical quality. These limitations hinder the scalability, fidelity and performance of vdW-based photonic components, especially in applications that rely on strong optical confinement or high-Q resonances.

To overcome these challenges, we developed a generally applicable nanofabrication strategy based on FIB lithography with Al passivation (inset of Fig. 1a; see Methods for details). The fabrication process begins with the mechanical exfoliation of vdW flakes[3], followed by a polydimethylsiloxane (PDMS)-assisted dry transfer[39]. A thin Al layer (~50 nm) is subsequently deposited, then direct-write FIB milling is applied to define arbitrary nanoscale patterns. The Al layer is finally removed by wet etching to reveal intact and well-patterned vdW structures (Supplementary Fig. 10). The Al layer serves two critical functions: protecting the underlying vdW materials from ion implantation damage[40,41] and mitigating surface charging to prevent pattern deformation during FIB milling. The surface passivation is especially crucial for preserving the optical performance, as even a single Ga-ion imaging scan can introduce severe crystal defects and increase scattering losses in waveguide and resonator devices. We implemented free-space measurements to demonstrate the Ga-ion-induced material degradation (Extended Data Fig. 1a,b; the measurement set-up is shown in Supplementary Fig. 1). Raman spectroscopy and the second-harmonic (SH) intensity confirm that samples processed with Al passivation retain superior crystalline and optical properties compared with their unprotected counterparts. Under the with-Al protection condition, Raman peaks are better resolved and the SH intensity is four times higher than in the without-Al case, both reflecting the change of the intrinsic properties from the Ga-ion irradiation. We emphasize that we did not use fabricated structures (for example, WGM microcavities) in these free-space experiments, so that the observed signal differences arise solely from material degradation and serve to demonstrate the protective function of the Al film.

By primarily using the physical fabrication methods, we avoid using many hazardous chemical etchants that risk substrate damage, rendering this method applicable across a broad range of vdW materials. Our method provides accurate pattern alignment and can be used to fabricate vdW nanostructures spanning from single-material systems to diverse vertically stacked, free-selection vdW heterostructures. The resolution achieved (sub-100 nm, as demonstrated by the fabrication of the line-space patterns shown in Extended Data Fig. 1c and the linewidth histogram in Supplementary Fig. 11) is comparable with that from electron-beam lithography, while eliminating the need for a hard mask and greatly simplifying the process flow.

Using the described fabrication protocol, we created a series of vdW-based photonic nanostructures—microdisks, photonic crystals and arrays of triangular resonators—from various materials, such as h-BN, MoS_2, GaSe and $NbOCl_2$ (Fig. 1b). The fabrication of complex geometries, including stacked heterostructures (for example, the $MoS_2/VOCl_2$-stacked microdisk in Fig. 1b) and institutional logos (see our universities' logos in Extended Data Fig. 1d), further highlights the precision and generality of the method. Taken together, our FIB-based fabrication strategy provides a robust, material-independent route for high-quality vdW photonic structures. It outlines a possible route towards reconfigurable and multifunctional vdW photonic integrated circuits that leverage the full material versatility of this platform.

High-Q vdW microcavities

The ability to fabricate ultralow-loss optical microcavities is essential for advancing integrated photonics. Among various resonant structures, WGM microcavities stand out for their ability to confine light within small mode volumes while maintaining ultrahigh Q factors, making them an excellent platform for enhancing light–matter interactions. To evaluate the quality of our fabrication approach, we constructed microcavities using various vdW materials transferred onto quartz substrates. The microdisks were designed with thicknesses of hundreds of nanometres and with radii spanning tens of micrometres to optimally support WGMs via total internal reflection. The Q factor, defined as the ratio of the energy stored in the cavity to the energy lost per optical cycle, was measured by coupling light into the microdisk via a tapered optical fibre with a U-shaped configuration (Supplementary Fig. 2). This set-up enables evanescent excitation and the comprehensive characterization of the WGMs. We used wavelength-tunable CW lasers to scan across broad spectral ranges, from the visible to the telecom bands. Transmission spectra for h-BN microdisks across these wavelengths are shown in Fig. 2a. At telecom bands, four transverse electric (TE) mode families are clearly identified, TE_{00}, TE_{10}, TE_{02} and TE_{01}. The corresponding field distributions simulated using COMSOL Multiphysics are plotted in the bottom right corner of Fig. 2a. Only TE modes were observed experimentally due to the high in-plane refractive index of h-BN ($n_{\parallel} \approx 2.20$), which strongly confines light in the cavity plane. By contrast, transverse magnetic modes, which have their electric field mainly oriented perpendicular to the microcavity plane, have a lower refractive index ($n_{\perp} \approx 1.58$) that fails to provide sufficient optical confinement, resulting in leaky modes with substantially reduced Q factors.

A closer view of the transmission spectra around the two modes TE_{00} and TE_{10} in the 1,550-nm band is shown in Fig. 2b. From these spectra, fairly high intrinsic Q factors of around 10^6 were obtained (see Methods and Supplementary Section IV for details of the characterization technique). Furthermore, a statistical survey of TE_{00} modes across the telecom band confirmed that these Q values were consistently achieved (Fig. 2c). Such high Q values, corresponding to a propagation loss of approximately 0.35 dB cm^{-1}, highlight the benefits of the atomic-level surface and smooth sidewalls of the microdisks. At this level, the scattering loss becomes the dominant contributor to the total optical loss, outweighing both material absorption and radiation leakage[42]. We experimentally observed a wavelength-dependent trend in Q, with higher Q values at longer wavelengths (Fig. 2d), consistent with theoretical predictions based on surface roughness scattering (Supplementary Section V). This trend underscores the critical role of our fabrication precision in reducing the scattering loss and enabling high-Q microcavities, while also highlighting the possibility of further improvements towards even better devices.

The demonstration of vdW microdisk resonators with $Q > 10^6$ confirms that our fabrication method enables vdW materials to fully exploit their intrinsic optical property advantages. The demonstrated

https://doi.org/10.1038/s41563-026-02574-x

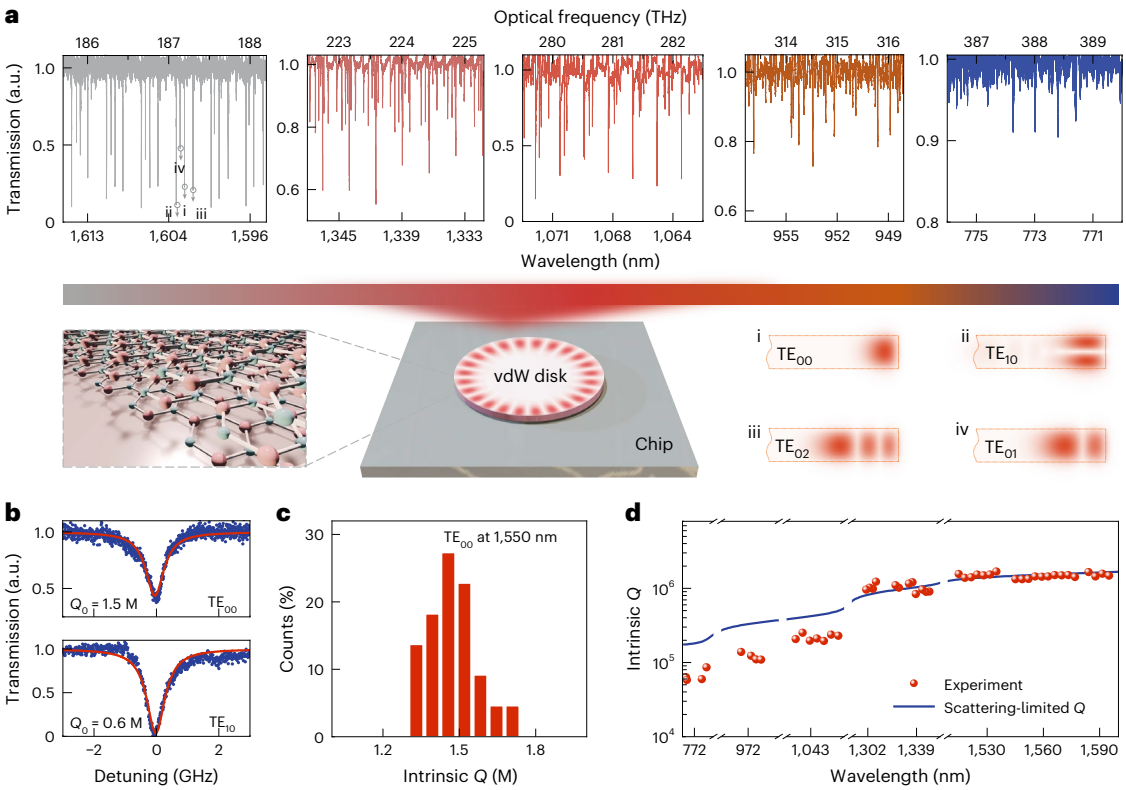

Fig. 2 | vdW whispering gallery microcavities with an ultrahigh *Q* factor. **a**, Top: broadband transmission spectra measured in different wavelength bands, showing cavity resonances across a wide spectral range. Grey arrows in the first spectrum mark four different mode families (TE_{00}, TE_{10}, TE_{02} and TE_{01}). Bottom left: schematic of the structure of the vdW material. Bottom middle: schematic of a vdW microcavity on a single chip supporting WGMs. Bottom right: numerically simulated electric field distributions corresponding to the WGM families (i to iv) shown in the first spectrum in the top panel. **b**, Typical transmission spectra of TE_{00} and TE_{10} modes for *Q*-factor extraction. Q_0, the intrinsic *Q* factor. **c**, Statistical distribution of the intrinsic *Q* factor of TE_{00} modes in the telecom band. **d**, Wavelength-dependent intrinsic *Q* factors measured over several spectral bands compared with theoretical predictions based on scattering loss from surface roughness.

performance surpasses that of many previous vdW-materials resonant systems by three orders of magnitude (Extended Data Fig. 2 and Supplementary Table 1). This high level is sustained across densely spaced modes spanning telecom to near-visible wavelengths. These microcavities provide a foundational building block for diverse photonic functionalities, including quantum light generation and low-threshold lasing. Note that h-BN has a bandgap of ~6 eV, thus offering a wide operational transparency window; however, the characterization of the h-BN microdisks beyond the telecom to near-visible ranges is limited by the wavelength coverage available in our laboratories. Nevertheless, the ability of various vdW materials to operate across a broad wavelength range—from infrared to ultraviolet—enhances their versatility for integration into multiband photonic systems.

Highly efficient CW-driven tunable SHG

Nonlinear optical processes lie at the heart of integrated photonics, as they enable frequency conversion, quantum light generation and reconfigurable signal processing. Leveraging the high-*Q* feature mentioned above, accompanied by the exceptionally high nonlinearity of vdW materials, we demonstrated highly efficient $\chi^{(2)}$- and $\chi^{(3)}$-nonlinear optical processes. We first demonstrated SHG, one of the most essential nonlinear optical processes, using GaSe microcavities with high second-order optical nonlinearity[43]. To do this, a CW fundamental wave (FW) was injected into the GaSe microdisk through a U-shaped fibre taper, and its frequency ω_p was gradually downtuned across the cavity modes. Owing to the interplay between the Kerr and thermo-optic effects, the transmission spectra exhibited characteristic non-Lorentzian 'thermal triangle' features (Fig. 3a). As the pump wavelength approached resonance, the resonance-enhanced intracavity power intensity led to a steep rise in SH emission at $2\omega_p$, which was collected vertically through an objective lens.

The SHG efficiency, measured as a function of pump power, exhibited a linear scaling in the weak-pump regime (Fig. 3b), consistent with theoretical expectations for the undepleted pump regime[44]. With increasing pump power (>100 mW), the efficiency slightly deviated from the theoretical line, which is attributed to a thermally induced change in the fibre–cavity coupling condition as the cavity temperature rises. Real-space imaging of the microdisk confirmed the spatial localization of the SH signal at the cavity perimeter (insets of Fig. 3b). Notably, the highest absolute SHG efficiency reached ~3.7 ± 0.1% at ~172 mW. The normalized efficiency in the undepleted regime was ~30% W^{-1}, an improvement of four orders of magnitude over previously reported vdW systems[45,46]. This notable improvement is attributed to the high *Q* of the FW cavity mode, as SHG efficiency scales quadratically with the *Q* factor of the FW mode[44].

Further, we demonstrated broadband SHG behaviour. By downscanning the FW frequency ranging from ~204 THz to 192 THz (correspondingly from 1,470 nm to 1,560 nm), we obtained an SH signal ranging from ~408 THz to 384 THz, as plotted in the top and bottom panels of Fig. 3c, respectively. The resulting SH peaks appeared at typical intervals of about 1.75 THz, corresponding to twice the FSR of the TE_{00} cavity mode family at the telecom band. Also note that some frequencies corresponding to FW resonances, for example, those near 390 THz and 400 THz, did not produce observable SHG peaks. This phenomenon is attributed to two primary factors: (1) mode crossings between distinct mode families led to reduced coupling efficiency and

https://doi.org/10.1038/s41563-026-02574-x

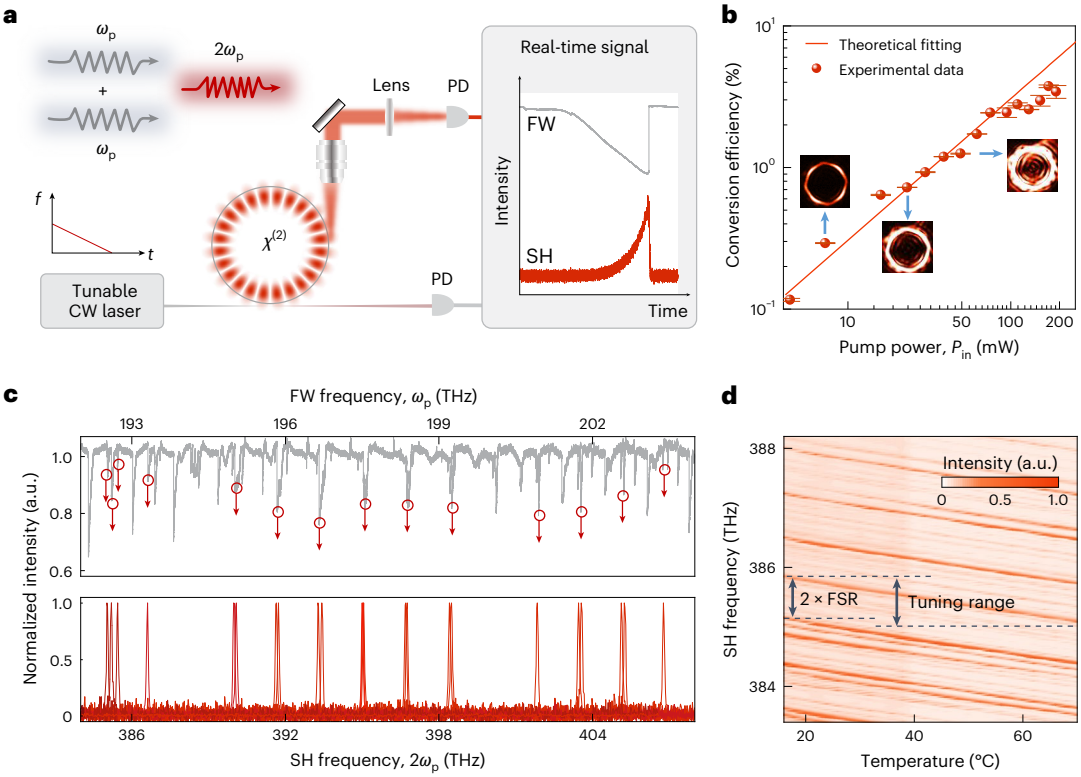

Fig. 3 | Highly efficient CW-driven tunable SHG in a GaSe microcavity. **a**, Experimental set-up for SHG measurement. A tunable CW laser is coupled via a fibre taper. Inset: SHG process and typical time-scan results. *f*, frequency. **b**, SHG conversion efficiency as a function of pump power. The results are the mean of three independent measurements. Insets: top-view images of the microdisk showing SH emission at different pump power levels. **c**, Broadband transmission FW spectrum (top) and the corresponding SH signal (bottom). Red circles mark the FW frequencies that generate SH signals. **d**, Thermally tunable SH frequency as a function of temperature ranging from 16 °C to 70 °C. Twice the FSR in the FW band (~0.70 THz) and the thermal-tuning SH range (~0.76 THz) are indicated for comparison. The GaSe microcavity radius was ~15 μm in **b**, 20 μm in **c** and 60 μm in **d**. PD, photodetector.

(2) momentum mismatch between the pump and SH light generated within the microcavity impeded efficient SHG.

The high-efficiency process was achieved without relying on double resonance or strict phase matching but, instead, through the combination of ultrahigh *Q* factors, strong second-order nonlinearity and large effective interaction volumes in vdW microcavities. These results indicate strong potential for further improvement once the phase-matching and double-resonance conditions are fully engineered. Moreover, this process is good for realizing a high-efficiency broadband nonlinear process owing to the released mode-sensitive phase-matching condition. Indeed, using the same GaSe material system with a large thermo-optic coefficient, we achieved thermally tunable SHG in a microdisk resonator, which presented obvious changes in the effective refractive index with temperature (Extended Data Fig. 3). This thermal tuning shifted the resonant frequencies of the cavity modes, thereby enabling tunability of broadband SHG. Figure 3d presents the collected results of generated SH light. The SH frequency spanned from ~383 THz to 388 THz for different substrate temperatures (16 °C to 70 °C). Notably, temperature tuning enabled a continuous SHG frequency scan of ~0.76 THz, which exceeds twice the FSR in the FW band (~0.70 THz). This indicates the potential of the GaSe microdisk to generate a widely tunable SHG signal within its optical transparency window. Such temperature-based control offers substantial potential for on-chip photonic applications, including wavelength-agile light sources, reconfigurable photonic circuits and integrated spectroscopy.

CW-driven SFG and OPA

Nonlinear processes, such as SFG and OPA, are critical for wavelength conversion, coherent signal generation and quantum optics. These processes typically require precise phase matching and high pump powers, which are difficult to achieve under CW excitation in vdW-materials platforms. Here we demonstrate both CW-driven SFG and OPA in vdW microcavities, which are enabled by high-*Q* confinement and strong intrinsic optical nonlinearity.

SFG is a second-order nonlinear optical process wherein two input photons of frequencies ω_1 and ω_2 interact to produce a photon at the sum frequency ($\omega_3 = \omega_1 + \omega_2$), as schematically illustrated in Fig. 4a. In our experiment, two independent CW lasers were tuned to resonate with the distinct modes of a GaSe microdisk at approximately 191.5 THz and 197.8 THz, respectively. These pumps were coupled into the microdisk via a tapered fibre and excited separate TE-mode resonances. The resulting SFG signal appeared at ~389.3 THz, and the accompanying SHG signals were observed near 382.7 THz and 395.9 THz (Fig. 4b). The observed slight deviations between the expected and measured frequencies are attributed to two factors: (1) thermal and Kerr-induced resonance shifts arising under a high intracavity intensity and (2) imperfect fulfilment of the frequency-matching condition. The clear spectral features confirm the successful generation of both SFG and SHG within the same microcavity. Notably, the SFG output remained robust under thermal tuning from 20 °C to 73 °C as it maintained a consistent signal intensity of ~1,100 counts over a tuning range of ~0.7 THz (Fig. 4c). This robust signal benefitted from two pump beams independently resonating with separate cavity modes, and the SFG photon was not confined by a narrow microcavity resonance.

Further, we exploited the $\chi^{(3)}$ nonlinearity of h-BN in a separate microdisk resonator to demonstrate the OPA process. In that process, two pump photons at frequency ω_p and one idler photon at ω_i generated a signal photon at $\omega_s = 2\omega_p - \omega_i$ while simultaneously amplifying the

https://doi.org/10.1038/s41563-026-02574-x

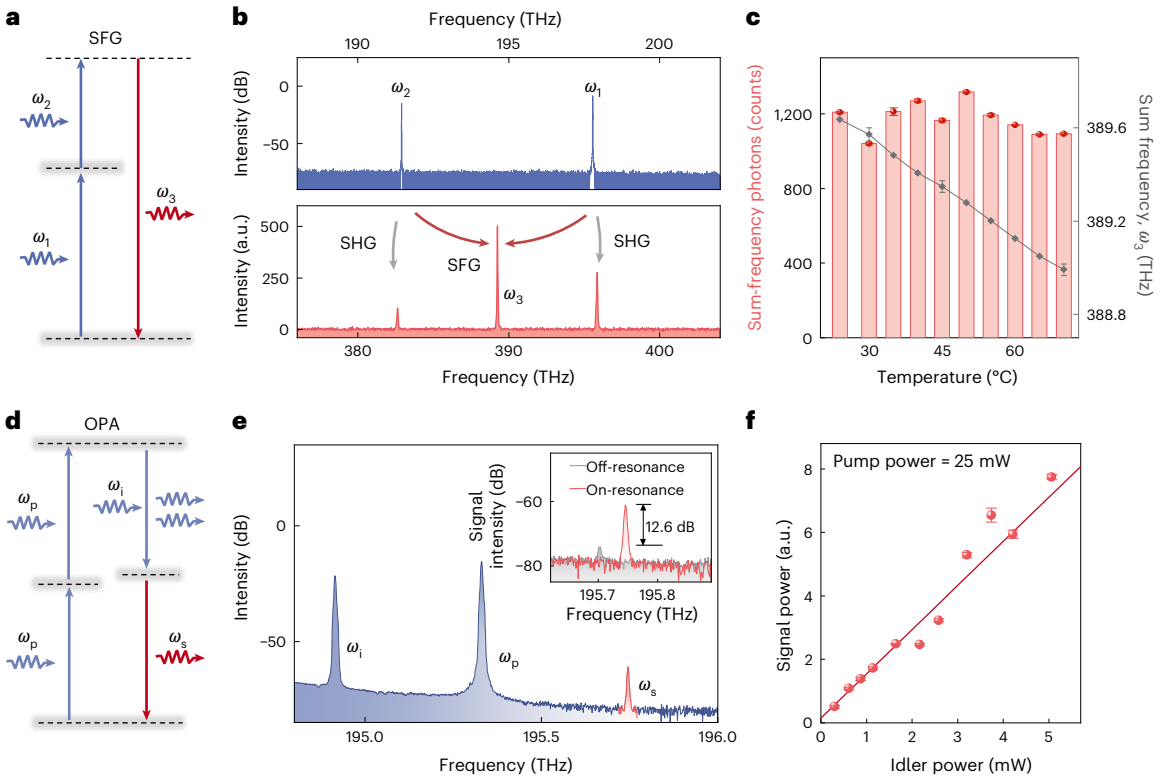

Fig. 4 | Demonstration of CW-driven SFG and OPA processes. a, Energy-level diagram illustrating an SFG process in a GaSe microcavity. Two input fields at ω_1 and ω_2 (blue) generate a sum-frequency signal at $\omega_3 = \omega_1 + \omega_2$ (red). **b**, Spectra showing the input FW beams (top) and the generated SHG and SFG signals (bottom). **c**, Thermally tunable SFG signal intensity (red bars) and its corresponding SFG frequency tuning (grey curve) over a temperature range of 20–73 °C. The radius of the GaSe microcavity was ~20 µm. Data are shown as mean ± standard deviation from four independent measurements. **d**, Energy-level diagram of a $\chi^{(3)}$ OPA process in an h-BN microcavity. ω_p, ω_i and ω_s denote the frequencies of the pump, idler and signal, respectively. **e**, Spectrum showing the pump, idler and signal light. Inset: zoom-in of the generated signal power when the pump light is on-resonance (red) and off-resonance (grey) with respect to the cavity mode. **f**, Dependence of the output signal power on the input idler power, with the pump power fixed at 25 mW. The radius of the h-BN microcavity was ~50 µm. Data are shown as mean ± standard deviation from three independent measurements.

idler wave (Fig. 4d). Experimentally, a strong pump at ~195.3 THz and a weaker idler at ~194.9 THz were coupled into the cavity. When the pump wave was on-resonance with a cavity mode, a new signal emerged near 195.7 THz (the red peak in Fig. 4e). A comparison between the on- and off-resonance conditions revealed a signal enhancement of ~12.6 dB (inset of Fig. 4e), confirming the resonance-assisted parametric gain. The output signal power exhibited a linear dependence on the idler input power, as expected for the OPA process (Fig. 4f). This demonstration establishes vdW microdisks as a viable platform for CW-driven nonlinear optical amplification. However, this amplification process is, at present, limited by a large detuning, which originates from the non-ideal cavity dispersion design. Implementing dispersion engineering to achieve the desired dispersion condition while taking the Kerr modulation into account could be a pathway to overcoming this limitation and enhancing the process.

Conclusion

In conclusion, we have introduced a high-precision nanostructuring technique for a wide range of vdW materials that enables the fabrication of diverse photonic components with exceptional optical quality. As a representative example, we realized h-BN microcavities supporting WGMs with intrinsic Q factors exceeding 10^6. Exploiting the high-Q resonances in a GaSe microcavity, we demonstrated CW-driven SHG with full FSR tunability. We finally reported efficient SFG and OPA, all achieved with CW excitations, an important advance over previous ultrafast-pulsed implementations. These findings address key limitations in nonlinear optical gain for vdW-based photonics and open avenues for energy-efficient light conversion on-chip.

Looking ahead, further optimization of the fabrication process to achieve higher Q cavities (Supplementary Section XIII), combined with carefully engineered cavity mode dispersion through geometric design and effective refractive index modulation, could substantially boost nonlinear optical performance under phase-matching conditions[44,47,48]. By combining high-Q resonances, exceptional nonlinearity and the potential for periodic poling[49], vdW-based resonant platforms hold substantial promise for applications such as quantum light sources[50], quantum logic gates[51] and ultra-sensitive sensors[52]. Beyond these, the integration of quantum emitters with vdW cavities offers a pathway to cavity-quantum electrodynamic regimes that would enable spontaneous emission control and strong-coupling dynamics demonstrations[29,53,54]. Furthermore, coupling ultralow-loss vdW structures with other resonant modes, such as plasmonic, phononic and excitonic platforms, may unlock new physical phenomena and application frontiers[55]. Overall, our results establish vdW materials not merely as functional overlays but as foundational building blocks for next-generation integrated photonics, thus opening pathways for exploring light–matter interactions and for realizing scalable, high-performance, versatile photonic devices with excellent capabilities.

Online content

Any methods, additional references, Nature Portfolio reporting summaries, source data, extended data, supplementary information, acknowledgements, peer review information; details of author contributions and competing interests; and statements of data and code availability are available at https://doi.org/10.1038/s41563-026-02574-x.

References

1. Geim, A. K. & Grigorieva, I. V. Van der Waals heterostructures. *Nature* **499**, 419–425 (2013).
2. Novoselov, K. S., Mishchenko, A., Carvalho, A. & Neto, A. H. C. 2D materials and van der Waals heterostructures. *Science* **353**, aac9439 (2016).
3. Novoselov, K. S. et al. Electric field effect in atomically thin carbon films. *Science* **306**, 666–669 (2004).
4. Bonaccorso, F., Sun, Z., Hasan, T. & Ferrari, A. C. Graphene photonics and optoelectronics. *Nat. Photonics* **4**, 611–622 (2010).
5. Chaves, A. et al. Bandgap engineering of two-dimensional semiconductor materials. *npj 2D Mater. Appl.* **4**, 29 (2020).
6. Balandin, A. A. Thermal properties of graphene and nanostructured carbon materials. *Nat. Mater.* **10**, 569–581 (2011).
7. Androulidakis, C., Zhang, K., Robertson, M. & Tawfick, S. Tailoring the mechanical properties of 2D materials and heterostructures. *2D Mater.* **5**, 032005 (2018).
8. Guo, Q. et al. Ultrathin quantum light source with van der Waals $NbOCl_2$ crystal. *Nature* **613**, 53–59 (2023).
9. Pelgrin, V., Yoon, H. H., Cassan, E. & Sun, Z. Hybrid integration of 2D materials for on-chip nonlinear photonics. *Light: Adv. Manuf.* **4**, 311–333 (2023).
10. Xia, F., Wang, H., Xiao, D., Dubey, M. & Ramasubramaniam, A. Two-dimensional material nanophotonics. *Nat. Photonics* **8**, 899–907 (2014).
11. Sun, Z., Martinez, A. & Wang, F. Optical modulators with 2D layered materials. *Nat. Photonics* **10**, 227–238 (2016).
12. Meng, Y. et al. Photonic van der Waals integration from 2D materials to 3D nanomembranes. *Nat. Rev. Mater.* **8**, 498–517 (2023).
13. Wu, S. et al. Monolayer semiconductor nanocavity lasers with ultralow thresholds. *Nature* **520**, 69–72 (2015).
14. Du, L. et al. Nonlinear physics of moiré superlattices. *Nat. Mater.* **23**, 1179–1192 (2024).
15. Basov, D., Fogler, M. & García de Abajo, F. Polaritons in van der Waals materials. *Science* **354**, aag1992 (2016).
16. Koppens, F. et al. Photodetectors based on graphene, other two-dimensional materials and hybrid systems. *Nat. Nanotechnol.* **9**, 780–793 (2014).
17. Yoon, H. H. et al. Miniaturized spectrometers with a tunable van der Waals junction. *Science* **378**, 296–299 (2022).
18. Cui, X. et al. Miniaturized spectral sensing with a tunable optoelectronic interface. *Sci. Adv.* **11**, eado6886 (2025).
19. Bogaerts, W. et al. Programmable photonic circuits. *Nature* **586**, 207–216 (2020).
20. Zotev, P. G. et al. Nanophotonics with multilayer van der Waals materials. *Nat. Photonics* **19**, 788–802 (2025).
21. Kim, S. All-2D material photonic devices. *Nanoscale Adv.* **5**, 323–328 (2023).
22. Yao, B. et al. Gate-tunable frequency combs in graphene–nitride microresonators. *Nature* **558**, 410–414 (2018).
23. Gu, T. et al. Regenerative oscillation and four-wave mixing in graphene optoelectronics. *Nat. Photonics* **6**, 554–559 (2012).
24. Maiti, R. et al. Strain-engineered high-responsivity $MoTe_2$ photodetector for silicon photonic integrated circuits. *Nat. Photonics* **14**, 578–584 (2020).
25. Datta, I. et al. Low-loss composite photonic platform based on 2D semiconductor monolayers. *Nat. Photonics* **14**, 256–262 (2020).
26. Weber, T. et al. Intrinsic strong light–matter coupling with self-hybridized bound states in the continuum in van der Waals metasurfaces. *Nat. Mater.* **22**, 970–976 (2023).
27. Verre, R. et al. Transition metal dichalcogenide nanodisks as high-index dielectric Mie nanoresonators. *Nat. Nanotechnol.* **14**, 679–683 (2019).
28. Zograf, G. et al. Combining ultrahigh index with exceptional nonlinearity in resonant transition metal dichalcogenide nanodisks. *Nat. Photonics* **18**, 751–757 (2024).
29. Ling, H., Li, R. & Davoyan, A. R. All van der Waals integrated nanophotonics with bulk transition metal dichalcogenides. *ACS Photonics* **8**, 721–730 (2021).
30. Zhang, H. et al. Hybrid exciton-plasmon-polaritons in van der Waals semiconductor gratings. *Nat. Commun.* **11**, 3552 (2020).
31. Kumar, P. et al. Light–matter coupling in large-area van der Waals superlattices. *Nat. Nanotechnol.* **17**, 182–189 (2022).
32. Lynch, J., Guarneri, L., Jariwala, D. & van de Groep, J. Exciton resonances for atomically-thin optics. *J. Appl. Phys.* **132**, 091102 (2022).
33. Brar, V. W., Sherrott, M. C. & Jariwala, D. Emerging photonic architectures in two-dimensional opto-electronics. *Chem. Soc. Rev.* **47**, 6824–6844 (2018).
34. Sung, J. et al. Room-temperature continuous-wave indirect-bandgap transition lasing in an ultra-thin WS_2 disk. *Nat. Photonics* **16**, 792–797 (2022).
35. Li, C. et al. Room-temperature near-infrared excitonic lasing from mechanically exfoliated InSe microflake. *ACS Nano* **16**, 1477–1485 (2021).
36. Popkova, A. A. et al. Nonlinear exciton-Mie coupling in transition metal dichalcogenide nanoresonators. *Laser Photonics Rev.* **16**, 2100604 (2022).
37. Zotev, P. G. et al. Van der Waals materials for applications in nanophotonics. *Laser Photonics Rev.* **17**, 2200957 (2023).
38. Munkhbat, B., Küçüköz, B., Baranov, D. G., Antosiewicz, T. J. & Shegai, T. O. Nanostructured transition metal dichalcogenide multilayers for advanced nanophotonics. *Laser Photonics Rev.* **17**, 2200057 (2023).
39. Frisenda, R. et al. Recent progress in the assembly of nanodevices and van der Waals heterostructures by deterministic placement of 2D materials. *Chem. Soc. Rev.* **47**, 53–68 (2018).
40. Giannuzzi, L. A. & Garrison, B. J. Molecular dynamics simulations of 30 and 2 keV Ga in Si. *J. Vac. Sci. Technol. A* **25**, 1417–1419 (2007).
41. Gierak, J. Focused ion beam technology and ultimate applications. *Semicond. Sci. Technol.* **24**, 043001 (2009).
42. Gao, M. et al. Probing material absorption and optical nonlinearity of integrated photonic materials. *Nat. Commun.* **13**, 3323 (2022).
43. Zhou, X. et al. Strong second-harmonic generation in atomic layered GaSe. *J. Am. Chem. Soc.* **137**, 7994–7997 (2015).
44. Guo, X., Zou, C.-L. & Tang, H. X. Second-harmonic generation in aluminum nitride microrings with 2500%/W conversion efficiency. *Optica* **3**, 1126–1131 (2016).
45. Trovatello, C. et al. Quasi-phase-matched up- and down-conversion in periodically poled layered semiconductors. *Nat. Photonics* **19**, 291–299 (2025).
46. Abdelwahab, I. et al. Giant second-harmonic generation in ferroelectric $NbOI_2$. *Nat. Photonics* **16**, 644–650 (2022).
47. Lu, J., Li, M., Zou, C.-L., Al Sayem, A. & Tang, H. X. Toward 1% single-photon anharmonicity with periodically poled lithium niobate microring resonators. *Optica* **7**, 1654–1659 (2020).
48. Wang, Z.-Y. et al. Toward ultimate-efficiency frequency conversion in nonlinear optical microresonators. *Sci. Adv.* **11**, eadu7605 (2025).
49. Chen, C. et al. Large-scale domain engineering in two-dimensional ferroelectric $CuInP_2S_6$ via giant flexoelectric effect. *Nano Lett.* **22**, 3275–3282 (2022).
50. Li, M. et al. Single-mode photon blockade enhanced by bi-tone drive. *Phys. Rev. Lett.* **129**, 043601 (2022).
51. Li, M. et al. Photon-photon quantum phase gate in a photonic molecule with $\chi^{(2)}$ nonlinearity. *Phys. Rev. Appl.* **13**, 044013 (2020).

52. Oh, S.-H. et al. Nanophotonic biosensors harnessing van der Waals materials. *Nat. Commun.* **12**, 3824 (2021).
53. Kim, G. et al. High-density, localized quantum emitters in strained 2D semiconductors. *ACS Nano* **16**, 9651–9659 (2022).
54. Kim, G. et al. Confinement of excited states in two-dimensional, in-plane, quantum heterostructures. *Nat. Commun.* **15**, 6361 (2024).
55. de Abajo, F. J. G. et al. Roadmap for photonics with 2D materials. *ACS Photonics* **12**, 3961–4095 (2025).

Methods

Device fabrication

The VdW materials used in this study were sourced from 2D Semiconductors and mechanically exfoliated onto PDMS substrates. Selected flakes were transferred onto quartz substrates using a deterministic dry-transfer method[3]. Atomic force microscopy (Bruker Dimension Icon) was used to characterize flake thickness. Before nanofabrication, samples were annealed under ~10^{-5} mbar at 170 °C for 2 h to improve surface cleanliness and adhesion. Then the samples were passivated with a 50-nm Al layer using physical vapour deposition (MASA IM-9912). The vdW materials were patterned via FIB (Helios Nanolab 600) using a programmed milling function (gallium ion beam). Finally, the Al passivation layer was removed by wet etching in dilute AZ 351B (Merck).

Q-factor characterization

The *Q* factors of the disk microcavities were measured across a broad spectral range. Tunable CW lasers were employed in six spectral regions (770 nm, 980 nm, 1,064 nm, 1,330 nm, 1,460 nm and 1,550 nm; DLC CTL series, TOPTICA Photonics; TLB-6712-P, Newport). Calibration was performed using a fibre-based Mach–Zehnder interferometer. The laser was frequency-modulated and injected into the microdisk through a tapered fibre. A Lorentzian-type transmission spectrum was observed near the resonance frequency. The corresponding linewidth κ was read over the scanning time with the calibrated Mach–Zehnder interferometer, which enabled us to extract the loaded *Q* factor $Q = \omega/\kappa$, where ω is the resonance frequency. The intrinsic *Q* factors were extracted via the loaded linewidth and the coupling efficiency, the detailed operation of which is given in Supplementary Section IV along with the calibration method.

Nonlinear optical processes in a microcavity

Three nonlinear optical processes—SHG, SFG and OPA—were demonstrated in this work. SHG operates in a GaSe microdisk with second-order nonlinearity under the non-depletion regime, with the process further enhanced by cavity mode confinement. The coupled-mode equation for the pump mode can be described as

$$\frac{da}{dt} = i\Delta_p a - \frac{\kappa_p}{2}a - i\sqrt{\kappa_{p,ex}}a_{in}, \tag{1}$$

where Δ_p denotes the pump-cavity detuning and $\kappa_p(\kappa_{p,ex})$ represents the total (external coupling) loss of the pump mode. The SH signal power can be written as

$$|b|^2 = M\frac{2\pi^2\omega_s^2|\chi^{(2)}|^2 Q_p^2}{\epsilon_0 c^3 n_p^2 n_s V_{eff}^2}|a|^4, \tag{2}$$

where *M* evaluates the field overlap between the FW mode and the SH free-space propagating field, $a_{in} = \sqrt{\kappa_{p,ex}P_{in}/\omega_p\hbar}$ represents the injected photon number. ϵ_0 is the vacuum permittivity and $\hbar$ is the reduced Plank constant. Q_p and V_{eff} denote the quality factor of the pump mode and the effective mode volumn. n_p (n_s) represents the effective refractive index of the pump (SH) light. SFG is realized using dual CW pumps tuned to distinct cavity modes, with both pump fields governed by equation (1) under the non-depletion regime. As for the OPA process with the third-order nonlinearity within an h-BN microdisk, the coupled-mode equations are

$$\begin{aligned}
\frac{da}{dt} &= i\Delta_p a - \tfrac{\kappa_p}{2}a - 2iga^* bc - i\sqrt{\kappa_{p,ex}}a_{in},\\
\frac{db}{dt} &= i\Delta_i b - \tfrac{\kappa_i}{2}b - iga^2c^* - i\sqrt{\kappa_{i,ex}}b_{in},\\
\frac{dc}{dt} &= i\Delta_s c - \tfrac{\kappa_s}{2}c - iga^2 b^*,
\end{aligned} \tag{3}$$

where a (a^*), b (b^*) and c (c^*) denote the photon number amplitude (and their conjugates) for the pump, idler and signal modes, respectively, and $b_{in} = \sqrt{\kappa_{i,ex}P_{in}/\omega_i\hbar}$ represents the injected idler photon number. g is the single-photon coupling strength. Δ_i (Δ_s) denotes the idler (signal)-cavity detuning, κ_i (κ_s) represents the total loss of the idler (signal) mode, and $\kappa_{i,ex}$ is the external coupling loss for the idler mode.

Reporting summary

Further information on research design is available in the Nature Portfolio Reporting Summary linked to this article.

Data availability

Source data are provided with this paper.

References

56. Sortino, L. et al. Optically addressable spin defects coupled to bound states in the continuum metasurfaces. *Nat. Commun.* **15**, 2008 (2024).
57. Fröch, J. E., Hwang, Y., Kim, S., Aharonovich, I. & Toth, M. Photonic nanostructures from hexagonal boron nitride. *Adv. Opt. Mater.* **7**, 1801344 (2019).
58. Khelifa, R. Coupling interlayer excitons to whispering gallery modes in van der Waals heterostructures. *Nano Lett.* **20**, 6155–6161 (2020).

Acknowledgements

We acknowledge helpful discussions with and suggestions from Q.-T. Cao, Q.-F. Yang, Y. Hu, Z. Liu, H.-J. Chen, X. Sui, J.-Y. Liu and S.-J. Tang. This project is supported by the National Key R&D Program of China (Grant Nos. 2023YFB2806702 and 2021ZD0301500), the National Natural Science Foundation of China (Grant Nos. 12293051 and 11825402), the Fundamental and Interdisciplinary Disciplines Breakthrough Plan of the Ministry of Education of China (JYB2025XDXM106), the Research Council of Finland (Grant Nos. 352780, 352930, 353364, 360411, 359009, 365686, 374168 and 367808), the Research Council of Finland Flagship Programme (Grant No. 320167, PREIN) and the ERC (Advanced Grant No. 834742, ATOP). We acknowledge the provision of facilities and technical support from the Otaniemi research infrastructure (OtaNano-Micronova Nanofabrication Centre). X. Cui acknowledges the Alfred Kordelin Foundation and the Walter Ahlström Foundation. This work is part of the Finnish Centre of Excellence in Quantum Materials (QMAT).

Author contributions

Y.-F.X. and Z.S. conceived the idea and supervised the project. Z.-Y.W. and H.-R.S. conducted the optical experiments and analysed the data. X. Cui, A.C.L. and N.S. developed the fabrication technique used in this work. X. Cheng and J.Y. fabricated the GaSe microdisks and improved the SHG efficiency during the revision processes. W.Z. and W.L. measured the refractive indices of the materials. H.K. and J.C.A.M. assisted with the fabrication and characterization of the microdisks. K. Lin measured the damage threshold of GaSe. Z.-Y.W., X. Cui and A.C.L. drafted the paper, with revisions provided by Y.-F.X., Z.S., Q.G. and K. Liu.

Funding

Open Access funding provided by Aalto University.

Competing interests

The authors declare no competing interests.

Additional information

Extended data is available for this paper at https://doi.org/10.1038/s41563-026-02574-x.

Supplementary information The online version contains supplementary material available at https://doi.org/10.1038/s41563-026-02574-x.

Correspondence and requests for materials should be addressed to Zhipei Sun or Yun-Feng Xiao.

Peer review information *Nature Materials* thanks Deep Jariwala and the other, anonymous, reviewer(s) for their contribution to the peer review of this work.

https://doi.org/10.1038/s41563-026-02574-x

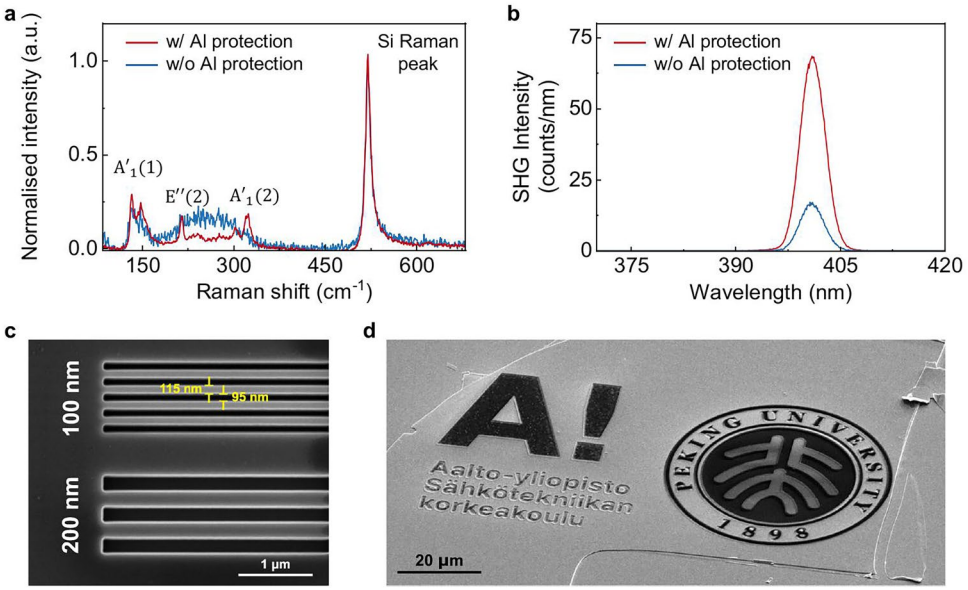

Extended Data Fig. 1 | FIB patterning and Al protection method. a, Raman spectra measured from GaSe fabricated with and without Al passivation. **b**, Measured SH intensity from GaSe fabricated with and without Al passivation. The results underscore the critical role of Al passivation in preserving the vdW material properties during FIB lithography. **c**, Resolution characterisation of the fabrication technique. The resolution refers to the smallest achievable half-pitch of a line-space pattern with 50% duty cycle. The smallest achievable individual feature can be much smaller than the resolution, and is limited by the magnitude of process errors. **d**, Logos of Aalto University (left) and Peking University (right) patterned on vdW materials, showcasing the ability to define arbitrary shapes. The Raman and SHG results are obtained from free-space measurements (the measurement setup shown in Fig. S1), without involvement of structure resonances (for example, WGMs); the observed signal differences therefore originate solely from material degradation and serve to demonstrate the protective role of the Al film.

https://doi.org/10.1038/s41563-026-02574-x

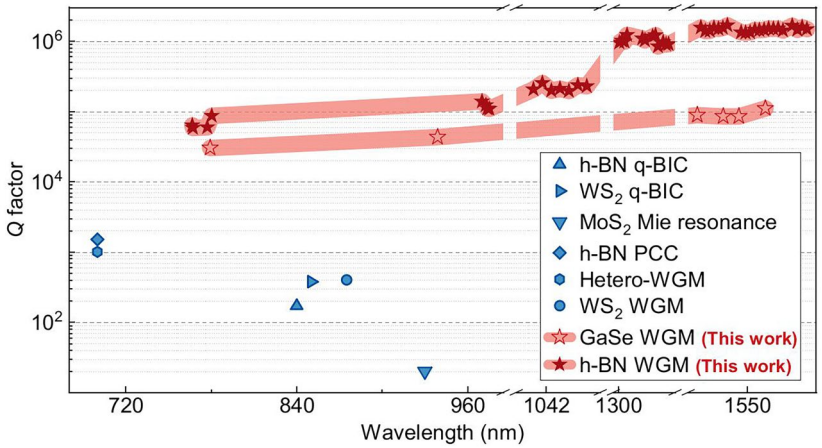

Extended Data Fig. 2 | Comparison of realised Q factors of resonators on vdW material platforms. Comparison encompasses multiple resonant modes: quasi-bound states in the continuum (q-BIC)[26,56], photonic crystal cavity (PCC)[57], Mie resonator[28] and WGM cavity[34,58], evaluated across the spectral range from 680 - 1600 nm.

https://doi.org/10.1038/s41563-026-02574-x

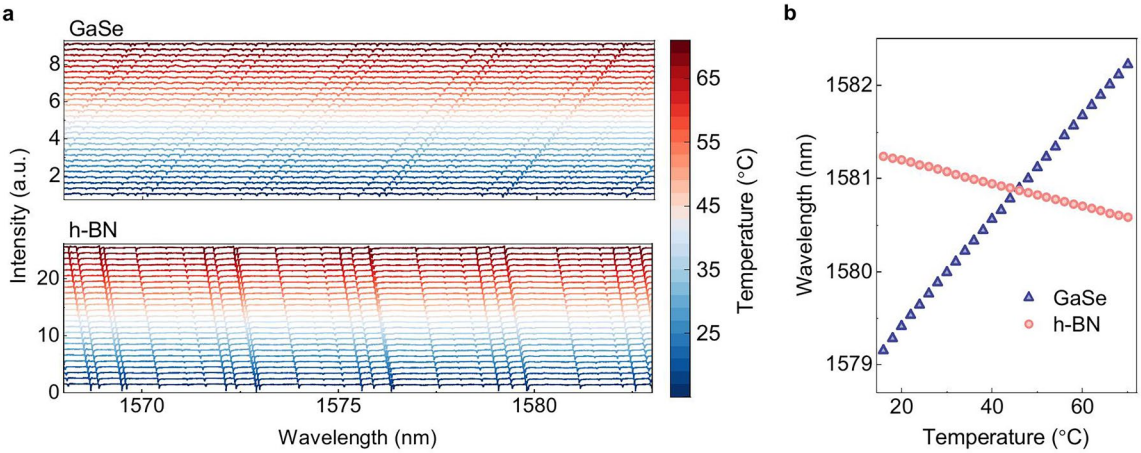

Extended Data Fig. 3 | Thermal tunability of WGMs with different vdW materials. a, Broadband transmission spectra for GaSe and h-BN microdisks at varying substrate temperatures. **b**, Temperature dependence of the resonance wavelength for the GaSe and h-BN microdisks extracted from **a**.

nature portfolio

Corresponding author(s): Sun Zhipei , Xiao Yun-Feng

Last updated by author(s): 2026/3/4

Reporting Summary

Nature Portfolio wishes to improve the reproducibility of the work that we publish. This form provides structure for consistency and transparency in reporting. For further information on Nature Portfolio policies, see our Editorial Policies and the Editorial Policy Checklist.

Statistics

For all statistical analyses, confirm that the following items are present in the figure legend, table legend, main text, or Methods section.

n/a	Confirmed	
☐	☒	The exact sample size (*n*) for each experimental group/condition, given as a discrete number and unit of measurement
☐	☒	A statement on whether measurements were taken from distinct samples or whether the same sample was measured repeatedly
☐	☒	The statistical test(s) used AND whether they are one- or two-sided *Only common tests should be described solely by name; describe more complex techniques in the Methods section.*
☐	☒	A description of all covariates tested
☒	☐	A description of any assumptions or corrections, such as tests of normality and adjustment for multiple comparisons
☐	☒	A full description of the statistical parameters including central tendency (e.g. means) or other basic estimates (e.g. regression coefficient) AND variation (e.g. standard deviation) or associated estimates of uncertainty (e.g. confidence intervals)
☒	☐	For null hypothesis testing, the test statistic (e.g. *F*, *t*, *r*) with confidence intervals, effect sizes, degrees of freedom and *P* value noted *Give P values as exact values whenever suitable.*
☒	☐	For Bayesian analysis, information on the choice of priors and Markov chain Monte Carlo settings
☒	☐	For hierarchical and complex designs, identification of the appropriate level for tests and full reporting of outcomes
☒	☐	Estimates of effect sizes (e.g. Cohen's *d*, Pearson's *r*), indicating how they were calculated

Our web collection on statistics for biologists contains articles on many of the points above.

Software and code

Policy information about availability of computer code

Data collection	Microsoft Office LTSC 2021
Data analysis	Origin 2023b

For manuscripts utilizing custom algorithms or software that are central to the research but not yet described in published literature, software must be made available to editors and reviewers. We strongly encourage code deposition in a community repository (e.g. GitHub). See the Nature Portfolio guidelines for submitting code & software for further information.

Data

Policy information about availability of data

All manuscripts must include a data availability statement. This statement should provide the following information, where applicable:

- Accession codes, unique identifiers, or web links for publicly available datasets
- A description of any restrictions on data availability
- For clinical datasets or third party data, please ensure that the statement adheres to our policy

Source data are provided with this paper.

Research involving human participants, their data, or biological material

Policy information about studies with human participants or human data. See also policy information about sex, gender (identity/presentation), and sexual orientation and race, ethnicity and racism.

Reporting on sex and gender	No relation.
Reporting on race, ethnicity, or other socially relevant groupings	No relation.
Population characteristics	No relation.
Recruitment	No relation.
Ethics oversight	No relation.

Note that full information on the approval of the study protocol must also be provided in the manuscript.

Field-specific reporting

Please select the one below that is the best fit for your research. If you are not sure, read the appropriate sections before making your selection.

☒ Life sciences ☐ Behavioural & social sciences ☐ Ecological, evolutionary & environmental sciences

For a reference copy of the document with all sections, see nature.com/documents/nr-reporting-summary-flat.pdf

Life sciences study design

All studies must disclose on these points even when the disclosure is negative.

Sample size	Our sample was fabricated by us. The content of the statistics is the optical properties of this sample. Three to four sets of signal intensities under the same conditions are taken and averaged.
Data exclusions	No relation.
Replication	Confirmed.
Randomization	No relation.
Blinding	No relation.

Reporting for specific materials, systems and methods

We require information from authors about some types of materials, experimental systems and methods used in many studies. Here, indicate whether each material, system or method listed is relevant to your study. If you are not sure if a list item applies to your research, read the appropriate section before selecting a response.

Materials & experimental systems

n/a	Involved in the study
☒	☐ Antibodies
☒	☐ Eukaryotic cell lines
☒	☐ Palaeontology and archaeology
☒	☐ Animals and other organisms
☒	☐ Clinical data
☒	☐ Dual use research of concern
☒	☐ Plants

Methods

n/a	Involved in the study
☒	☐ ChIP-seq
☒	☐ Flow cytometry
☒	☐ MRI-based neuroimaging

Plants

Seed stocks	No relation.
Novel plant genotypes	No relation.
Authentication	No relation.